

1 **Assessment of ICESat-2 sea ice surface classification with Sentinel-2 imagery:**
2 **implications for freeboard and new estimates of lead and floe geometry**

3 A. A. Petty^{1,2}, M. Bagnardi^{2,3}, N. Kurtz¹, R. Tilling^{1,2}, S. Fons^{2,4}, T. Armitage, C. Horvat⁵, R.
4 Kwok⁶

5 ¹ Earth System Interdisciplinary Center, University of Maryland, College Park, MD, USA

6 ² NASA Goddard Space Flight Center, Greenbelt, MD, USA

7 ³ ADNET Systems, Inc., Bethesda, MD, USA

8 ⁴ Department of Atmospheric and Oceanic Sciences, University of Maryland, College Park, MD,
9 USA

10 ⁵ Brown University, Providence, RI, USA.

11 ⁶ University of Washington, Seattle, WA, USA.

12

13 Corresponding author: Alek A. Petty (alek.a.petty@nasa.gov)

14 **Key points**

- 15 • Specular leads in ICESat-2 show strong agreement with leads observed in coincident
16 Sentinel-2 imagery.
- 17 • The scenes provide further evidence of the misclassification of dark leads, which are no
18 longer used to derive freeboard in ICESat-2 data.
- 19 • We produce preliminary estimates of lead fraction and chord length across the Arctic and
20 Southern Ocean.

21 **Abstract**

22 NASA's Ice, Cloud, and Land Elevation Satellite-2 (ICESat-2) mission launched in September
23 2018 and is now providing high-resolution surface elevation profiling across the entire globe,
24 including the sea ice cover of the Arctic and Southern Oceans. For sea ice applications,
25 successfully discriminating returns between sea ice and open water is key for accurately
26 determining freeboard, the extension of sea ice above local sea level, and new information
27 regarding the geometry of sea ice floes and leads. We take advantage of near-coincident optical
28 imagery obtained from the European Space Agency (ESA) Sentinel-2 (S-2) satellite over the

29 Western Weddell Sea of the Southern Ocean in March 2019 and the Lincoln Sea of the Arctic
30 Ocean in May 2019 to evaluate the surface classification scheme in the ICESat-2 ATL07 and
31 ATL10 sea ice products. We find a high level of agreement between the ATL07 (specular) lead
32 classification and visible leads in the S-2 imagery in these two scenes across all six ICESat-2
33 beams, increasing our confidence in the freeboard products and deriving new estimates of the sea
34 ice state. The S-2 overlays provide additional evidence of the misclassification of dark leads,
35 which are no longer used to derive sea surface in the third release (r003) ICESat-2 sea ice
36 products. We show estimates of lead fraction and more preliminary estimates of chord length (a
37 proxy for floe size) using two metrics for classifying sea surface (lead) segments across both the
38 Arctic and Southern Ocean for the first winter season of data collection.

39 **1. Introduction**

40 NASA's Ice, Cloud, and Land Elevation Satellite-2 (ICESat-2) is a new satellite mission
41 providing unprecedented (high resolution and accuracy) profiling of the Earth's surface,
42 especially over the high-latitude polar regions. ICESat-2 was launched successfully from
43 Vandenberg Air Force Base on September 15th, 2018 and started acquiring science quality data
44 on October 14th, 2018. A description of the ICESat-2 mission design and objectives can be
45 found in Markus et al., (2017) and Neumann et al., (2019).

46 ICESat-2 consists of a bespoke photon-counting Advanced Topographic Laser Altimeter
47 System (ATLAS) - a low pulse-energy laser split into a novel six-beam configuration of three
48 beam pairs (a strong and a weak beam). At orbital velocities, ATLAS generates individual laser
49 footprints of ~14 m (in diameter) on the Earth's surface. The high pulse repetition rate of 10 kHz
50 means laser pulses are separated by only 70 cm along-track; a much higher resolution and
51 sampling than NASA's previous laser altimetry mission ICESat (Zwally et al., 2002). ICESat-2
52 samples year-round and has only experienced minimal downtime since launch.

53 Various data products are now being generated routinely from IS2 which are publicly
54 disseminated through the National Snow and Ice Data Center (NSIDC,
55 <https://nsidc.org/data/icesat-2>). The primary science data product from ICESat-2 is the Level 2A
56 ATL03 geolocated photon heights (Neumann et al., 2019) from which most of the higher-level
57 science products are derived. For sea ice users, the primary products of interest are the L3A

58 along-track sea ice height and type (ATL07, <https://nsidc.org/data/ATL07>) and freeboard
59 (ATL10, <https://nsidc.org/data/ATL10>) products. The first winter-season of Arctic sea ice
60 heights and freeboards (October 2018 to March 2019) were presented in (Kwok, et al., 2019).
61 Sea ice thickness has been estimated from these freeboards using external snow loading
62 estimates from the NASA Eulerian Snow on Sea Ice Model (NESOSIM) and modified versions
63 of the Warren climatology (Petty et al., 2020) and through the combination of ICESat-2 laser
64 (total) freeboard with CryoSat-2 radar (ice) freeboard to derive snow depth and freeboard
65 concurrently (Kwok et al., 2020). The surface heights and freeboards were assessed against
66 coincident airborne elevation data collected by NASA's Operation IceBridge (Kwok et al.,
67 2019b). The along-track heights generated from the Airborne Topographic Mapper (ATM,
68 Studinger, 2014) flown on OIB showed strong agreement with ATL07-derived heights, while the
69 derived freeboard from ATM showed only small (0-4 cm) differences with ATL10 freeboards,
70 depending on the method used to derive and compare freeboard. Coincident imagery obtained
71 during the OIB surveys by the Continuous Airborne Mapping By Optical Translator (CAMBOT)
72 alluded to erroneous classification of dark leads in the presence of clouds (Kwok et al., 2020b).
73 Dark leads are still included in the latest (r003) ATL07 sea ice height and surface classification
74 product release, but have now been excluded from the derivation of freeboard in the latest (r003)
75 ATL10 product release (the ATL07 and ATL10 products are described more in the following
76 section). The Kwok et al., (2020b) study highlighted the significant utility of coincident high-
77 resolution imagery for better understanding the performance of the ICESat-2 sea ice surface
78 classification algorithm. The assessment, however, was hindered by the high consolidation of the
79 ice pack in the region profiled during the spring 2019 OIB campaign, limiting the number of
80 leads/open water segments and the quality of the freeboard estimates due to the lack of reliable
81 sea surface tie-points.

82 The main objective of this study is to further assess the performance of the surface
83 classification scheme in ATL07 for discriminating between sea ice and open water. We take
84 advantage of near-coincident optical imagery from the Sentinel-2 satellite mission to assess this
85 specific aspect of the ATL07 algorithm performance. Successfully discriminating returns
86 between sea ice and open water has benefits beyond deriving freeboard. Additional metrics for
87 understanding the sea ice state include concentration, lead fraction (or density) and floe size. In
88 the marginal seas, where waves can break up and fracture the ice (Horvat et al., 2020 and

89 references therein), ice floes are thought to be smaller and less concentrated/consolidated (a
90 higher lead fraction) than within the pack ice. The geometry of floes and leads is an important
91 control on the strength of sea ice and its thermodynamic response to forcing (Feltham, 2005;
92 Horvat et al., 2016), particularly in marginal, coastal, and seasonally-ice-covered seas. The floe
93 size distribution (Rothrock & Thorndike, 1984) is increasingly being introduced into sea ice
94 components of climate models (Bateson et al., 2020; Roach et al., 2018), but only limited basin-
95 scale observational constraints exist to-date, e.g. estimates derived from ESA's CryoSat-2 radar
96 altimeter for the Arctic Ocean only (Horvat et al., 2019). ICESat-2 offers the exciting potential to
97 provide new observational estimates of the floe size distribution, benefiting from the small
98 footprint, high precision and along-track sampling rate across the multiple beams. Satellite tracks
99 (e.g. those from ICESat-2) will profile floes at random angles and cross sections of the floe. The
100 along-track length of a floe measured by satellite is commonly referred to as a chord length. A
101 collection of floe chord lengths can provide statistics of floe geometry, e.g. moments of the floe
102 size distribution and the open water fraction, under certain assumptions about the underlying floe
103 geometry (Horvat et al., 2019).

104 The coincident S-2 scenes provide the ideal means for assessing new lead fraction and
105 chord length estimates from ICESat-2 data, complementing the freeboard/thickness estimates
106 already being generated. We choose to discuss lead fraction instead of sea ice concentration as
107 concentration/extent was discussed in Horvat et al., (2020) and an assessment/comparison with
108 the commonly used passive microwave-derived concentrations (taking into account the
109 significant sampling differences) is beyond the scope of this study.

110 **2. Data**

111 **2.1 ATL07 sea ice heights and surface classification**

112 We primarily use data from the ICESat-2 ATL07 sea ice height and type product. A full
113 description of the ATL07 product can be found in the Algorithm Theoretical Basis Document
114 (ATBD, Kwok et al., 2019c) and the recent changes to this algorithm for r003 are discussed
115 more in Kwok et al., (2020b), so here we provide only a basic overview of the methodology
116 relevant to the results/discussion presented in this study.

117 ATL07 is generated by aggregating 150 photons from the ATL03 geolocated photon
118 product (Neumann et al., 2019) independently along each of the six beams. The beams are
119 arranged in ‘strong’ and ‘weak’ beam pairs with each beam pair separated by ~3.3 kilometers in
120 the across-track direction and the strong/weak beams separated by ~90 m across-track and ~2.5
121 km along-track. A surface finding routine (ATL07/10 ATBD r003 section 4.2) first windows the
122 photon heights around an expected sea surface then extracts a best-guess Gaussian height
123 distribution (convolved with the expected system response) to the photon height histogram to
124 determine 1) a single segment height, 2) an associated quality flag based on the goodness of fit
125 and 3) associated metrics including photon rate. The heights are expressed relative to the WGS84
126 ellipsoid with the mean sea surface (MSS) and various time-variable geophysical corrections
127 removed: ocean tides, solid earth tides, ocean loading, solid earth pole tides, inverted barometer.
128 Surface-classified height segments are produced for each of the six beams (three strong and weak
129 pairs) independently. The photon rates of the strong beam are roughly 4 times higher than those
130 of the weak beam, which results in mean segment lengths of ~15 m for the strong beam and ~60
131 m for the weak beam (Kwok et al., 2019). Adding the individual laser footprint size of ~14 m to
132 the segment length provides an estimate of the spatial resolution of the segments (i.e. a mean of
133 ~30 m x 15 m for the strong beam and 75 m x 15 m for the weak beam).

134 An empirically based decision-tree algorithm is used to discriminate the returns between
135 sea ice and open water (Kwok et al., 2016). The empirical thresholds were determined
136 principally by 1) data collected in campaigns prior to the launch of ICESat-2 by the Multiple
137 Altimeter Beam Experimental Lidar (MABEL) - a test-bed instrument for ICESat-2 (McGill et
138 al., 2013); and 2) post-launch evaluation of the ATLAS performance. The three inputs to this
139 decision tree (and the physical justifications) are as follows:

- 140 1. Photon rate (photon returns per laser pulse, the apparent reflectivity of the surface).
- 141 2. Width of the Gaussian fit to the photon height distribution (the small-scale surface
142 roughness).
- 143 3. Background rate (deviations compared to the photon rate indicate shadows, specular
144 reflections and/or atmospheric contamination).

145 The result of the decision tree determines the radiometric surface type (*height_segment_type* in
146 the product) which includes the following surfaces: clouds, ice (gray, rough, snow covered),

147 specular lead and dark leads (smooth and rough). This is considered the winter-time decision
148 tree. As discussed in the introduction, in the latest ATL07/10 data release (r003), dark leads were
149 dropped from the derivation of sea surface due to issues with cloud attenuation, so now only
150 specular leads are used for deriving sea surface and freeboard (Kwok et al., 2020b).

151 Due to the expected uncertainty in this radiometric surface classification approach (Kwok
152 et al., 2016), a further filtering is applied based on the local height distribution:

153 4. Local height filter, based on the distribution of local (10 km) smooth height segments
154 (h_{sm}) – segments with a Gaussian width < 0.13 m. Specifically the lead segment
155 height must be between the minimum of the smooth heights (h_{sm_min}) and the
156 maximum of either the 2nd percentile of the smooth heights or $h_{sm_min} + 2 \sigma$ where $\sigma =$
157 2-3 cm, the expected uncertainty in surface height over smooth surfaces.

158 The result of the radiometric decision tree and local height filter sets the sea surface
159 height flag (ssh_flag , $1 = sea\ ice$, $0 = open\ water$). Sea surface segments are considered
160 candidate leads for deriving freeboard in ATL10. Note that the summertime (non-winter)
161 decision tree simply extends the classification of ice, specular leads and dark leads as potential
162 melt ponds (not a feature of this analysis).

163 Freeboards are calculated in ATL10 in 10 km along-track sections based on a reference
164 sea surface derived from the available lead/sea surface segment heights. Consecutive lead
165 segments are grouped together to reduce noise in the individual sea surface estimates before a
166 single reference sea surface estimate is produced for each 10 km section. A further filtering is
167 applied to ensure that the 10 km sections are at least 25 km away from the coast and have a
168 concentration (from passive microwave data) $> 50\%$ - i.e. within the pack ice and away from
169 regions thought to be more affected by waves. The 10 km reference sea surface heights must also
170 lie within a set height window relative to the MSS (± 0.5 m for the Arctic and ± 1 m for the
171 Southern Ocean) and differences between consecutive sea surface heights must be relatively
172 small (see the ATL07/10 ATBD for more details). After the filtering, *candidate leads* are set as
173 leads for use in deriving freeboard ($ssh_flag = 2$) and freeboard segments are derived by
174 differencing the heights of the sea ice surface from the local reference sea surface height. More
175 detail about the methodology is given in Kwok et al., (2019b) and Kwok et al., (2020b).

176 **2.2 Sentinel-2 imagery**

177 Sentinel-2 is a constellation of two twin satellites, Sentinel-2A (S-2A) and Sentinel-2B
178 (S-2B), operated by the European Space Agency (ESA) and launched in June 2015 and March
179 2017, respectively. The satellites host the MultiSpectral Instrument (MSI), which provides 13
180 reflective-wavelength bands in the wavelength region between 443 nm and 2202 nm (visible,
181 near-infrared, short-wave infrared). Depending on the band, spatial resolution varies between 10,
182 20, and 60 m, and scenes are ~ 110 km x 110 km. For a given area, the shift by 180 degrees
183 between the two sun-synchronous polar orbits and a 290 km wide swath guarantee a revisit time
184 of 5 days at the equator, which improves to one image per day at higher latitudes due to
185 overlapping swaths with different viewing angles. Systematic global coverage of land surfaces
186 and coastal waters by S-2 imagery is available between 84 °N and 56 °S. However, additional
187 imagery is available near and over coastal regions of Antarctica, up to 73 °S.

188 We searched for coincident S-2 and ICESat-2 data over sea-ice covered portions of the
189 Arctic and Southern oceans. Our search algorithm matched the footprint of all S-2 images with a
190 nominal cloud coverage of less than 10% acquired during fall, winter, and spring months (fall
191 2018 to spring 2019) within the search regions (Arctic: Sep-May / Antarctic: Mar-Nov) with the
192 ICESat-2 reference ground track (RGT) times and locations (data from [https://icesat-
193 2.gsfc.nasa.gov/science/specs](https://icesat-2.gsfc.nasa.gov/science/specs)). We searched for overlapping data pairs with an acquisition time
194 difference of less than 2 hours to mitigate for ice drift. The selected images were checked for
195 quality, presence/absence of sea ice, actual cloud cover, and for the extent of the overlap with
196 ICESat-2 data, to obtain a catalog of data pairs suitable for our analyses. No images for winter
197 months (e.g. December/January in the Northern Hemisphere) are available due to the lack of sun
198 illumination. The optimal scenes found in this search were a ~ 50 km section in the Lincoln Sea
199 of the Arctic Ocean in May 2019 (i.e. the end of winter, time difference of 94 minutes) and the
200 Western Weddell Sea of the Southern Ocean in March 2019 (i.e. the start of the austral winter,
201 time difference of only 7 minutes), as shown in Figure 1. This Arctic Ocean scene occurs late in
202 the winter/spring season, after typical dates of melt onset in the Arctic. However, the location is
203 in the coldest/thickest ice of the Arctic and no surface melt is visible in the imagery. Visual
204 inspection of the scenes showed good coincidence and no obvious issues of drift misalignment.

205 **3. Methods**

206 **3.1 Classification evaluation**

207 To compare the IS-2 ATL07/10 data with the S-2 imagery we use a simple nearest
 208 neighbor interpolation scheme (the nearest geocoded pixel of the imagery to the given ATL07/10
 209 beam segment) to produce a coincident profile of S-2 surface reflectance. In particular, we use
 210 the red band, which is available at the highest 10 m spatial resolution and convert the Digital
 211 Number (DN) from Level-2A surface reflectance data products to spectral radiance (DN/10,000).
 212 We compare these profiles qualitatively as the lack of perfect time coincidence with the imagery,
 213 together with the possible impact of ice drift and the contrasting resolutions of the data, make it
 214 challenging to carry out a more robust quantitative assessment.

215 **3.2 Lead fraction**

216 To estimate lead fraction, we take the segment length weighted ratio of sea surface
 217 segments to the total length of valid segments in 10 km along-track sections across the combined
 218 three strong beams (we combine data from the 3 beams before sectioning the data). Note that the
 219 IS-2 measurements include three beam pairs spread over ~6.6 km across-track, so for this to be
 220 treated as a two-dimensional lead fraction estimate one needs to assume that the underlying ice is
 221 isotropic and homogenous over this 10 km x 6.6 km window, something we plan to test more in
 222 future work. The along-track lead fraction is calculated as

$$223 \quad L_f = \frac{\sum_{N_{sl}} l_s^i}{\sum_{N_{all}} l_s^i}, \quad (1)$$

224 where l_s is the segment length, N_{all} is the total number of ice and lead segments in the given
 225 section (10 km along-track in this study), N_{sl} is the total number of lead segments (specular only
 226 in r003) and i is the height segment index.

227 The ATL07/10 sea surface classification approach is designed to be strict – i.e. possible
 228 leads are potentially thrown away by the height percentile filter (step 4 in Section 2.1) to reduce
 229 the likelihood of ice segments being erroneously used to derive a reference sea surface. This
 230 approach makes sense when one considers the high sensitivity of the freeboard estimate to errors
 231 in the reference sea surface height calculation. However, for ice floe/lead geometry analyses,

232 such a strict filter could result in an underestimate of lead fraction (and an overestimate of chord
233 length, discussed in the following section). We therefore adopt two approaches for deriving lead
234 fraction: i) L_f^{v1} where we use the ATL07 sea surface flag for candidate leads ($ssh_flag = 1$) and
235 ii) L_f^{v2} where we use the ATL07 specular lead classification ($2 \leq height_segment_type \leq 5$)
236 together with a less strict 10 km local height percentile filter (20% instead of 2%, see step 4 in
237 Section 2.1) to determine the sea surface segments. In summary L_f^{v1} is derived using the
238 ssh_flag from the product, whereas L_f^{v2} is derived using a higher 20% local height filter. This is
239 a relatively crude way of exploring the sensitivity of these lead estimates to the underlying
240 classification algorithm which we will aim to expand on in future work.

241 **3.3 Chord length**

242 To calculate chord length, we devised a simple algorithm that splits the along-track
243 segment data into floe (or chord) groups based on the sea surface classification flag. The sea
244 surface segments are discarded. Similar to lead fraction, we use two approaches here; C_l^{v1}
245 utilizes the sea surface flag (ssh_flag) and C_l^{v2} uses the sea surface classification derived in this
246 study using the 20% local height filter. In both cases a ‘floe group’ needs to include at least 3
247 height segments and have a maximum spacing between consecutive segments less than 300 m.
248 300 m is the upper end of the tail of the distribution of segment lengths for the strong beams
249 (Kwok et al., 2019). Data gaps between segments are caused primarily by atmospheric scattering
250 (e.g. by clouds), which could result in erroneously high chord lengths, especially as clouds can
251 form preferentially over leads (although this is still being debated, e.g. Li et al., 2020). We also
252 discard any floe groups which are smaller than 60 m, which we take to be the minimum resolved
253 chord length due to considerations of footprint size and segment length, and groups which are
254 longer than 50 km. We add 15 m, the approximate photon footprint resolution, to all groups to
255 finally derive estimates of chord length. We run this analysis for each of the three strong beams
256 independently.

257 Note that we do not provide estimates of lead length in this study as estimates were provided
258 in Kwok et al., (2019) and this is thought to depend more on the resolution of the ATL07 data, so
259 investigations focused on the underlying ATL07 algorithm may be needed to produce more
260 reliable lead length estimates in future work.

261 For both the lead fraction and chord length estimates, we bin the along-track data to a 25 km
262 x 25 km polar stereographic grid (EPSG:3411 for the Arctic and EPSG:3412 for the Southern
263 Ocean) using data collected from the first Arctic (November 1, 2018 to April 30, 2019) and
264 austral (May 1, 2019 to September 30, 2019) winters.

265 **4. Results**

266 **4.1 Comparisons with Sentinel-2 imagery**

267 The S-2/ATL07 comparison for the ~50 km profile within the western Weddell Sea on
268 March 17th, 2019 is shown in Figure 2. This cropped S-2 image depicts a scene of mixed ice
269 surfaces - large consolidated floes, small broken up floes, and the occasional lead opening. It also
270 features very flat/thin ice for the first ~20 km and thicker/rougher ice (relative heights ~2/2.5 m
271 higher) for the remaining 30 km along-track. The final ~1 km of the scene features clouds, as can
272 be seen more clearly in the zoomed-out Figure 1. The ATL07 radiometric surface classification
273 scheme detected 218 specular lead segments and 8 dark lead segments for this scene, with 196
274 candidate (and indeed utilized) sea surface segments. The ATL07/10 lead classification shows
275 strong agreement with the S-2 imagery. As most of the lead segments are specular, the photon
276 rate shows corresponding spikes in these same locations, along with drops in the background rate
277 (as expected from background photons scattering away from the detector over specular surfaces).
278 The scene highlights the ability of ICESat-2 to detect both narrow (10s of meters) and wide
279 (100s of meters) openings in the ice cover. Dark lead classified segments are produced at ~7 km
280 and ~46 km along-track, with both appearing erroneous. The latter coincides clearly with the
281 presence of clouds in the S-2 imagery, further confirmed by the attenuation in photon rate around
282 this part of the scene, similar to the Operation IceBridge comparisons given in Kwok et al.,
283 (2020b). The ~7 km along-track dark lead is harder to diagnose, as this is associated with a sharp
284 drop in photon rate, as one would expect from a lead, but no obvious lead or cloud is visible in
285 the imagery. The derived lead fractions and chord lengths in this scene are also shown in Figure

286 2 (panel 6). The lead fractions are estimated as 1.47% (v_1) and 1.64% (v_2), while the mean chord
287 lengths are estimated as 2.76 km (v_1) and 2.32 km (v_2).

288 The S-2/ATL07 comparison for the ~50 km profile within the Lincoln Sea, Arctic Ocean
289 on May 25th, 2019 is shown in Figure 3. The S-2 image depicts a scene of large consolidated
290 floes, small broken up floes/leads, but also a much larger (> 1 km) lead opening. No clouds are
291 visible in the imagery (or implied by attenuations in the photon rate). The heights extend from
292 just over 0 m to ~2-2.5 m. The ATL07 radiometric surface classification scheme detected 166
293 specular leads and 0 dark leads for this scene, with 73 candidate (and again utilized) sea surface
294 segments. The ATL07/10 lead classification again shows strong agreement with the S-2 imagery.
295 Zooming in on the large lead in the S-2 image (not shown) highlights the presence of young ice
296 formation on the right (further along-track) side of the lead, which explains some of the drops in
297 photon rate and the absence of lead classifications. It is encouraging to note that the refrozen
298 lead of low height/freeboard at ~2 km along-track is not classified as a specular or dark lead. The
299 lead fractions for this scene are estimated as 2.12% (v_1) and 6.45% (v_2), while the chord lengths
300 are estimated as 1.83 km (v_1) and 2.13 km (v_2). The difference between the v_1 and v_2 estimates
301 are higher, and we can see this is mainly driven by the inclusion (or absence) of the segments
302 within the large lead opening. Including the extra sea surface segments by using a higher (20%)
303 height threshold in v_2 increases lead fractions, as expected, however also results in the more
304 counter intuitive result of increasing the mean chord length as the ice floe groupings remain too
305 small to be classified as a floe and are simply discarded. At ~10 km along-track, the S-2 scene
306 shows some small but highly consolidated ice floes, with no leads detected, highlighting the
307 challenge of lead/floe detection in the more consolidated ice regimes.

308 Further examples for these two scenes of both the strong and weak beams are given in the
309 Supplementary Information (Figures S1 to S10). These additional beam comparisons show again
310 a remarkably high level of agreement with the S-2 imagery in terms of the lead classification and
311 further examples of lead fraction and chord length estimates. No obvious degradation of the
312 classification performance is visible in the weak beam comparisons, although we generally see
313 fewer leads and lower lead fractions than with the strong beams.

314 4.2 Basin scale assessments

315 To better understand the sea ice classification and to provide context for the basin-scale
316 lead fraction/chord length estimates shown next, we first show basin-scale maps of key lead
317 classification metrics from ATL07 across the Arctic and Southern Ocean for the winter study
318 periods (Arctic: November 1, 2018 to April 30, 2019; Southern Ocean: May 1 2019 to
319 September 30, 2019). Figure 4 shows the radiometric lead fraction compared to all (segment
320 length weighted) segments, the ratio of radiometric specular lead segments to dark lead
321 segments, the fraction of specular lead segments that become sea surface segments ($ssh_flag > 0$)
322 and the fraction of sea surface (lead) segments compared to all segments – i.e. the lead fraction.
323 The radiometric lead and sea surface lead segments generally follow the spatial pattern expected
324 from our past knowledge of the sea ice state, increases in leads (declines in concentration)
325 towards the ice edge. In both hemispheres dark leads make up a significant (~50%) fraction of
326 the total number of radiometric leads. In both hemispheres a significant (>70%) fraction of the
327 specular leads pass the height filter and are assigned as sea surface segments. There is a clear
328 increase in the fraction of discarded specular leads along the ice edge in both hemispheres, but
329 also within the Canadian Arctic Archipelago. As ATL10 applies a stricter 50% concentration
330 filter from passive microwave data to avoid wave contamination (ATL07 uses 15%), and a 25
331 km coastal mask, many of these regions adjacent to the ice edge (in both hemispheres) and near
332 coastlines will not be processed into freeboard. Sea ice concentrations from the monthly (final
333 and near-real time) NSIDC Climate Data Record (CDR, Meier et al., 2017; Meier et al., 2017)
334 averaged over this same time period across both hemispheres are given in Figure 5 for context.

335 Figure 6 shows the 25 km x 25 km gridded lead fractions calculated using the ssh_flag
336 (L_f^{v1} , as in Figure 4d), and also using the 20% height filter (L_f^{v2}). L_f^{v2} consistently results in
337 higher lead fractions as expected, especially around the ice edge. We also note the increased lead
338 fractions in areas of known polynya formation - the North Water Polynya to the northwest of
339 Greenland and, to a lesser degree, Terra Nova Bay Polynya in the northern Ross Sea. Neither are
340 as visible in the passive microwave-derived concentrations (Figure 5). Mean Arctic Ocean lead
341 fraction are given as 1.06 % (L_f^{v1}) and 1.80 % (L_f^{v2}). Mean Southern Ocean lead fractions are
342 given as 0.66% (L_f^{v1}) and 1.24% (L_f^{v2}). The Southern Ocean lead fractions, while lower on
343 average, show increased lead fractions within the pack ice (compare with sea ice concentration in

344 Figure 5), especially in the eastern Southern Ocean. This is expected considering the open ocean
345 boundaries and the general divergent (away from the coast) Antarctic ice drifts. The results also
346 highlight the sensitivity of these estimates to this one aspect of the ATL07 lead finding
347 algorithm. Lead fractions within the pack ice of the Central Arctic are very low ($< 1\%$) which we
348 discuss more in the discussion/summary section.

349 Figure 7 shows the 25 km gridded chord lengths calculated using the *ssh_flag* (C_l^{v1}) and
350 the 20% height filter (C_l^{v2}). Mean Arctic Ocean chord lengths are given as 5.56 km (C_l^{v1}) and
351 5.23 km (C_l^{v1}). Mean Southern Ocean chord lengths are given as 5.43 km (C_l^{v1}) and 4.55 km
352 (C_l^{v2}). As in the lead fractions, there is high spatial variability not captured by these simple
353 hemispheric means. Lower chord lengths are produced within the eastern Arctic Ocean
354 (compared to the western Arctic Ocean) and also in the eastern Southern Ocean (compared to the
355 western Southern Ocean). The spatial variability is generally higher than the lead fraction as only
356 small changes in lead fraction can have a large impact on the derived chord lengths. The Arctic
357 shows a sharp increasing gradient within the more central Arctic region. Chord lengths are high
358 (consistently greater than 10 km) in the central Arctic, which we discuss more in the following
359 section.

360 Figure 8 shows the probability distribution of the individual chord lengths for the Arctic
361 and Southern Ocean using the C_l^{v1} and C_l^{v2} chord length estimates. The data are plotted on a
362 log-log scale to highlight the power law nature of the underlying distributions. The consistency
363 of the distributions across hemispheres and lead finding algorithm ($v1$ and $v2$) is encouraging.
364 The distributions become more variable at the tail of the distribution (> 10 km) due to the lower
365 sampling rate of these higher chord lengths. While log-log distributions can help visually
366 highlight power-law like behavior in empirical data, more robust statistical tests are needed to
367 truly test for whether data is well characterized by a power-law, especially due to the issues with
368 the less well-observed tails of the distribution (Clauset et al., 2009; Stern et al., 2018, Horvat et
369 al., 2019). We plan to explore this in future work as we compare against the chord length
370 estimates from other observed data, as discussed below.

371 **5. Discussion and summary**

372 The coincident Sentinel-2 (S-2)/ICESat-2 scenes provide crucial validation of the
373 ICESat-2 sea ice classification procedure, with the caveat that these represent only a small

374 fraction of the available sea ice data produced from ICESat-2 to-date. The specular lead
375 classification in the sea ice products shows strong agreement with the imagery across all beams,
376 while the small quantity of dark leads found in these scenes generally appear erroneous,
377 providing further evidence to that presented in Kwok et al., (2020b) of their more uncertain
378 reliability. More coincident S-2 scenes across different sea ice regimes (time and space) would
379 help provide further insight into the potential utility of the dark leads, especially as they make up
380 a significant fraction (~50-60%) of the total number of radiometric leads detected by the current
381 ATL07 algorithm. As discussed in Kwok et al., (2020b), the exclusion of dark leads from the
382 freeboard calculation has the downside of reducing coverage, especially in some of the more
383 consolidated sea ice regimes, providing motivation for continued study to ensure that this
384 exclusion is not overly restrictive.

385 It is interesting to note that the ATL07 segments over the relatively wide (> 1 km) lead in
386 our Arctic Ocean S-2 scene (Figure 3) were consistently classified as specular. Intuitively we
387 might expect this to be considered a ‘dark lead’ as the larger opening increases the fetch, but in-
388 fact the returns are consistently specular, until the photon rate drops drastically (to less than that
389 over the snow covered ice) as the ice starts to refreeze, with these segments classified as ice.
390 Similarly, the very thin cracks shown in the imagery (on the order of meters to tens of meters, i.e.
391 the segment resolution of the ATL07 data) were consistently classified as ice. It is unclear from
392 the S-2 imagery (10 m resolution) the extent to which these leads/cracks have refrozen. Higher
393 resolution imagery (e.g. from Digital Globe’s Worldview imagery) could provide useful further
394 insight here and will be explored in future work.

395 The local height filter included in the lead (sea surface) finding algorithm further limits
396 the number of leads identified. This appears reasonable when the goal is accurately determining
397 a reference sea level for freeboard but less ideal for deriving sea ice state information, e.g. lead
398 fraction and chord length. This study presented a crude approach to relax this height filter
399 (increasing the percentile threshold from 2% to 20%), which is worthy of further investigation as
400 we seek to increase the utility of the ICESat-2 sea ice data.

401 Validation, or at least comparisons, of our basin-scale ICESat-2 estimates of lead fraction
402 and chord length with existing observational estimates are still needed. Basin-scale lead fraction
403 estimates have been produced from various satellite sensors, e.g. NASA’s Moderate Resolution

404 Imaging Spectroradiometer (MODIS) (Hoffman et al., 2019; Willmes & Heinemann, 2016) and
405 Advanced Microwave Scanning Radiometer (AMSR-E) (Röhrs & Kaleschke, 2012), and also
406 ESA'S CryoSat-2 and Envisat radar altimeters (Röhrs & Kaleschke, 2012; Tilling et al., 2019).
407 Chord length distributions have also been produced from a compilation of more sporadic
408 satellite/airborne imagery estimates (Stern et al., 2018). However, comparisons with these data
409 are hindered by the considerable differences in spatial/temporal sampling, and also the different
410 interpretations and definitions of leads across sensors and algorithms. As discussed earlier, the
411 lead classification algorithm in ATL07 appears to require clear sections of open water to trigger
412 a specular lead classification. Therefore, newly refrozen leads, which may be defined as leads in
413 other (generally coarser resolution) products, may be simply classified as ice. The radar
414 altimeter-derived estimates of lead fraction and chord length from CryoSat-2 (Tilling et al., 2019,
415 Horvat et al., 2019) provide arguably the most similar dataset for comparison/assessment. The
416 CryoSat-2 lead fractions and chord lengths shown in Tilling et al., (2019) appear consistently
417 higher and lower, respectively, than the ICESat-2 results presented here. For example, Tilling et
418 al., (2019, Figure 1) shows the percentage of CryoSat-2 waveforms classified as lead (a quantity
419 related to, but not the same as lead fraction) as ~10 % in the Central Arctic but up to ~60 % in
420 the more peripheral seas, while the chord lengths (Tilling et al., 2019, Figure 2) are ~3 km in the
421 Central Arctic and ~1 km in the peripheral seas. In contrast, the chord lengths presented in this
422 study are consistently > 10 km within the Central Arctic. There is better agreement on the
423 general spatial pattern of increasing lead fractions/decreasing chord lengths in the peripheral
424 seas, however. Radar altimeters such as CryoSat-2 are highly sensitive to the presence of
425 specular leads within the radar swath and have the added benefit of being largely unaffected by
426 clouds. However, the CryoSat-2 footprint is much larger (~400 m along track and up to ~15 km
427 across track) than ICESat-2 (mean of ~30 m x 15 m for a given ATL07 strong beam segment).
428 Future work will aim to better assess, and hopefully reconcile, the lead fraction and chord length
429 estimates from these two missions, taking these significant sampling differences into account.
430 We also hope to explore further statistical testing of the power-law hypothesis for the floe length
431 distribution, which was recently challenged in Horvat et al., (2019) using CryoSat-2 chord length
432 estimates. This reconciliation is further motivated by the need to provide reliable observational
433 constraints on the floe size distributions being incorporated into sea ice components of Global

434 Climate Models (Horvat, et al., 2019). Airborne data from NASA's Operation IceBridge
435 campaigns, which combine high-resolution imagery and laser altimetry, should prove invaluable.

436 Our hope is that ICESat-2 sea ice data can be used to provide routine, and reliable, basin-
437 scale measurements of lead fraction, ice concentration and chord length estimates, in addition to
438 its primary mission requirement of delivering accurate estimates of sea ice height and freeboard.
439 Additional ICESat-2 sea ice algorithm testing and development is needed to further improve the
440 classification accuracy, which can be guided by additional comparisons with imagery (satellite
441 and airborne) and other airborne and satellite datasets. The ICESat-2 lead classification
442 algorithm utilizes fixed empirical thresholds (discussed in Section 2.1) which can easily be
443 tuned/calibrated as needed, as can other elements of the algorithm including the height percentile
444 threshold (which we simply explored in this study) and the photon aggregations. These
445 thresholds also need to be better explored in terms of appropriate strong/weak beam differences.
446 Efforts are also on-going to provide further insight into the dark leads and their potential
447 reintroduction by utilizing a new cloud filter in the sea ice algorithm (Kwok et al., 2020b).
448 However, this assumes that the dark lead classifications unaffected by clouds are more reliable,
449 which is still unclear. The results and discussion presented here also raise the issue of how best
450 to classify newly refrozen leads or gray ice in the sea ice products, or even where exactly to draw
451 the line between sea ice and open water – another key consideration as we seek to increase the
452 utility of the ICESat-2 sea ice products.

453 **Acknowledgements**

454 We would like to thank the entire ICESat-2 project for their continued efforts in
455 delivering and maintaining the high-quality sea ice data analyzed in this study.

456 **Data availability**

457 Sentinel-2 imagery was derived from Copernicus data obtained at
458 <https://schihub.copernicus.eu>. The ICESat-2 ATL07 (sea ice height and type) and ATL10
459 (freeboard) data products used here are available through the NSIDC (<https://nsidc.org/data/atl07>
460 & <https://nsidc.org/data/atl10>). Our lead fraction and chord length data will be made available
461 through the NASA Goddard Space Flight Center's Cryospheric Sciences Lab website on
462 completion of peer review.

463 **References**

- 464 Bateson, A. W., Feltham, D. L., Schröder, D., Hosekova, L., Ridley, J. K., & Aksenov, Y.
465 (2020). Impact of sea ice floe size distribution on seasonal fragmentation and melt of
466 Arctic sea ice. *The Cryosphere*, *14*(2), 403–428. <https://doi.org/10.5194/tc-14-403-2020>
- 467 Clauset, A., Shalizi, C. R., & Newman, M. E. J. (2009). Power-law distributions in empirical
468 data. *SIAM Review*, *51*(4), 661–703. <https://doi.org/10.1137/070710111>
- 469 Feltham, D. L. (2005). Granular flow in the marginal ice zone. *Philosophical Transactions of the*
470 *Royal Society A: Mathematical, Physical and Engineering Sciences*, *363*(1832), 1677–
471 1700. <https://doi.org/10.1098/rsta.2005.1601>
- 472 Hoffman, J. P., Ackerman, S. A., Liu, Y., & Key, J. R. (2019). The Detection and
473 Characterization of Arctic Sea Ice Leads with Satellite Imagers. *Remote Sensing*, *11*(5),
474 521. <https://doi.org/10.3390/rs11050521>
- 475 Horvat, C, Roach, L. A., Tilling, R., Bitz, C. M., Fox-Kemper, B., Guider, C., et al. (2019).
476 Estimating the sea ice floe size distribution using satellite altimetry: theory, climatology,
477 and model comparison. *The Cryosphere*, *13*(11), 2869–2885. [https://doi.org/10.5194/tc-](https://doi.org/10.5194/tc-13-2869-2019)
478 [13-2869-2019](https://doi.org/10.5194/tc-13-2869-2019)
- 479 Horvat, C., Blanchard-Wrigglesworth, E., & Petty, A. (2020). Observing Waves in Sea Ice With
480 ICESat-2. *Geophysical Research Letters*, *47*(10), e2020GL087629.
481 <https://doi.org/10.1029/2020GL087629>
- 482 Horvat, C., Tziperman, E., & Campin, J.-M. (2016). Interaction of sea ice floe size, ocean eddies,
483 and sea ice melting. *Geophysical Research Letters*, *43*(15), 8083–8090.
484 <https://doi.org/10.1002/2016GL069742>

- 485 Kwok, R., Cunningham, G. F., Hoffmann, J., & Markus, T. (2016). Testing the ice-water
486 discrimination and freeboard retrieval algorithms for the ICESat-2 mission. *Remote*
487 *Sensing of Environment*, 183, 13–25. <https://doi.org/10.1016/j.rse.2016.05.011>
- 488 Kwok, R., Cunningham, G., Hancock, D., Ivanoff, A., & Wimert, J. (2019). Ice, Cloud, and Land
489 Elevation Satellite-2 Project: Algorithm Theoretical Basis Document (ATBD) for Sea Ice
490 Products,. https://icesat-2.gsfc.nasa.gov/science/data_products.
- 491 Kwok, R., Kacimi, S., Markus, T., Kurtz, N. T., Studinger, M., Sonntag, J. G., et al. (2019).
492 ICESat-2 surface height and sea-ice freeboard assessed with ATM lidar acquisitions from
493 Operation IceBridge. *Geophysical Research Letters*, 44, 11228– 11236.
494 <https://doi.org/10.1029/2019GL084976>
- 495 Kwok, R., Markus, T., Kurtz, N. T., Petty, A. A., Neumann, T. A., Farrell, S. L., et al. (2019).
496 Surface Height and Sea Ice Freeboard of the Arctic Ocean From ICESat-2:
497 Characteristics and Early Results. *Journal of Geophysical Research: Oceans*, 124(10),
498 6942–6959. <https://doi.org/10.1029/2019JC015486>
- 499 Kwok, R., Kacimi, S., Webster, M. A., Kurtz, N. T., & Petty, A. A. (2020). Arctic Snow Depth
500 and Sea Ice Thickness From ICESat-2 and CryoSat-2 Freeboards: A First Examination.
501 *Journal of Geophysical Research: Oceans*, 125(3), e2019JC016008.
502 <https://doi.org/10.1029/2019JC016008>
- 503 Kwok, R., Petty, A. A., Bagnardi, M., Kurtz, N. T., Cunningham, G. F., & Ivanoff, A. (2020).
504 Refining the sea surface identification approach for determining freeboards in the
505 ICESat-2 sea ice products. *The Cryosphere Discussions*, 1–18. [https://doi.org/10.5194/tc-](https://doi.org/10.5194/tc-2020-174)
506 2020-174

- 507 Li, X., Krueger, S. K., Strong, C., Mace, G. G., & Benson, S. (2020). Midwinter Arctic leads
508 form and dissipate low clouds. *Nature Communications*, *11*(1), 206.
509 <https://doi.org/10.1038/s41467-019-14074-5>
- 510 Markus, T., Neumann, T., Martino, A., Abdalati, W., Brunt, K., Csatho, B., et al. (2017). The
511 Ice, Cloud, and land Elevation Satellite-2 (ICESat-2): Science requirements, concept, and
512 implementation. *Remote Sensing of Environment*, *190*, 260–273.
513 <https://doi.org/10.1016/j.rse.2016.12.029>
- 514 McGill, M., Markus, T., Scott, V. S., & Neumann, T. (2013). The Multiple Altimeter Beam
515 Experimental Lidar (MABEL): An Airborne Simulator for the ICESat-2 Mission. *Journal*
516 *of Atmospheric and Oceanic Technology*, *30*(2), 345–352.
517 <https://doi.org/10.1175/JTECH-D-12-00076.1>
- 518 Meier, W. N., Fetterer, F., & Windnagel, A. K. (2017). Near-Real-Time NOAA/NSIDC Climate
519 Data Record of Passive Microwave Sea Ice Concentration, Version 1.
520 <https://doi.org/10.7265/N5FF3QJ6>
- 521 Meier, W. N., Fetterer, F., Savoie, M., Mallory, S., Duerr, R., & Stroeve, J. (2017).
522 NOAA/NSIDC Climate Data Record of Passive Microwave Sea Ice Concentration,
523 Version 3. <https://doi.org/10.7265/N59P2ZTG>
- 524 Neumann, T. A., Martino, A. J., Markus, T., Bae, S., Bock, M. R., Brenner, A. C., et al. (2019).
525 The Ice, Cloud, and Land Elevation Satellite – 2 mission: A global geolocated photon
526 product derived from the Advanced Topographic Laser Altimeter System. *Remote*
527 *Sensing of Environment*, *233*, 111325. <https://doi.org/10.1016/j.rse.2019.111325>

- 528 Petty, A. A., Kurtz, N. T., Kwok, R., Markus, T., & Neumann, T. A. (2020). Winter Arctic Sea
529 Ice Thickness From ICESat-2 Freeboards. *Journal of Geophysical Research: Oceans*,
530 *125*(5), e2019JC015764. <https://doi.org/10.1029/2019JC015764>
- 531 Roach, L. A., Horvat, C., Dean, S. M., & Bitz, C. M. (2018). An Emergent Sea Ice Floe Size
532 Distribution in a Global Coupled Ocean-Sea Ice Model. *Journal of Geophysical*
533 *Research: Oceans*, *123*(6), 4322–4337. <https://doi.org/10.1029/2017JC013692>
- 534 Röhrs, J., & Kaleschke, L. (2012). An algorithm to detect sea ice leads by using AMSR-E
535 passive microwave imagery. *The Cryosphere*, *6*(2), 343–352. [https://doi.org/10.5194/tc-](https://doi.org/10.5194/tc-6-343-2012)
536 [6-343-2012](https://doi.org/10.5194/tc-6-343-2012)
- 537 Rothrock, D. A., & Thorndike, A. S. (1984). Measuring the sea ice floe size distribution. *Journal*
538 *of Geophysical Research: Oceans*, *89*(C4), 6477–6486.
539 <https://doi.org/10.1029/JC089iC04p06477>
- 540 Stern, H. L., Schweiger, A. J., Zhang, J., & Steele, M. (2018). On reconciling disparate studies of
541 the sea-ice floe size distribution. *Elem Sci Anth*, *6*(1), 49.
542 <https://doi.org/10.1525/elementa.304>
- 543 Studinger, M. (2014). IceBridge Narrow Swath ATM L1B Elevation and Return Strength,
544 Version 2. Boulder, Colorado USA. NSIDC: National Snow and Ice Data Center.
545 <https://doi.org/10.5067/CXEQS8KVIXEI>.
- 546 Tilling, R., Ridout, A., & Shepherd, A. (2019). Assessing the Impact of Lead and Floe Sampling
547 on Arctic Sea Ice Thickness Estimates from Envisat and CryoSat-2. *Journal of*
548 *Geophysical Research: Oceans*, *124*(11), 7473–7485.
549 <https://doi.org/10.1029/2019JC015232>

550 Willmes, S., & Heinemann, G. (2016). Sea-Ice Wintertime Lead Frequencies and Regional

551 Characteristics in the Arctic, 2003–2015. *Remote Sensing*, 8(1), 4.

552 <https://doi.org/10.3390/rs8010004>

553 Zwally, H. J., Schutz, B., Abdalati, W., Abshire, J., Bentley, C., Brenner, A., et al. (2002).

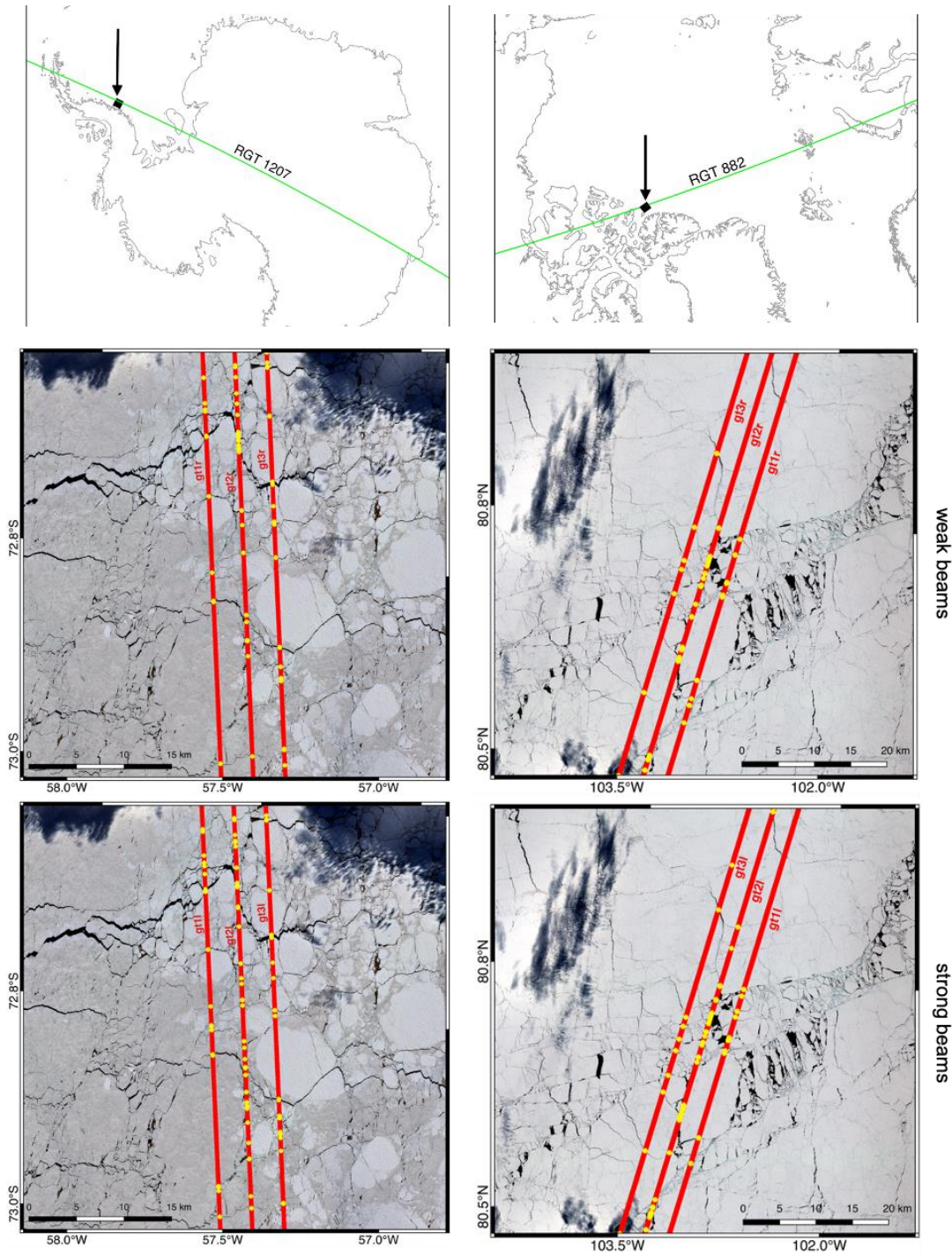
554 ICESat's laser measurements of polar ice, atmosphere, ocean, and land. *Journal of*

555 *Geodynamics*, 34(3–4), 405–445. [https://doi.org/10.1016/S0264-3707\(02\)00042-X](https://doi.org/10.1016/S0264-3707(02)00042-X)

556

557

Figures

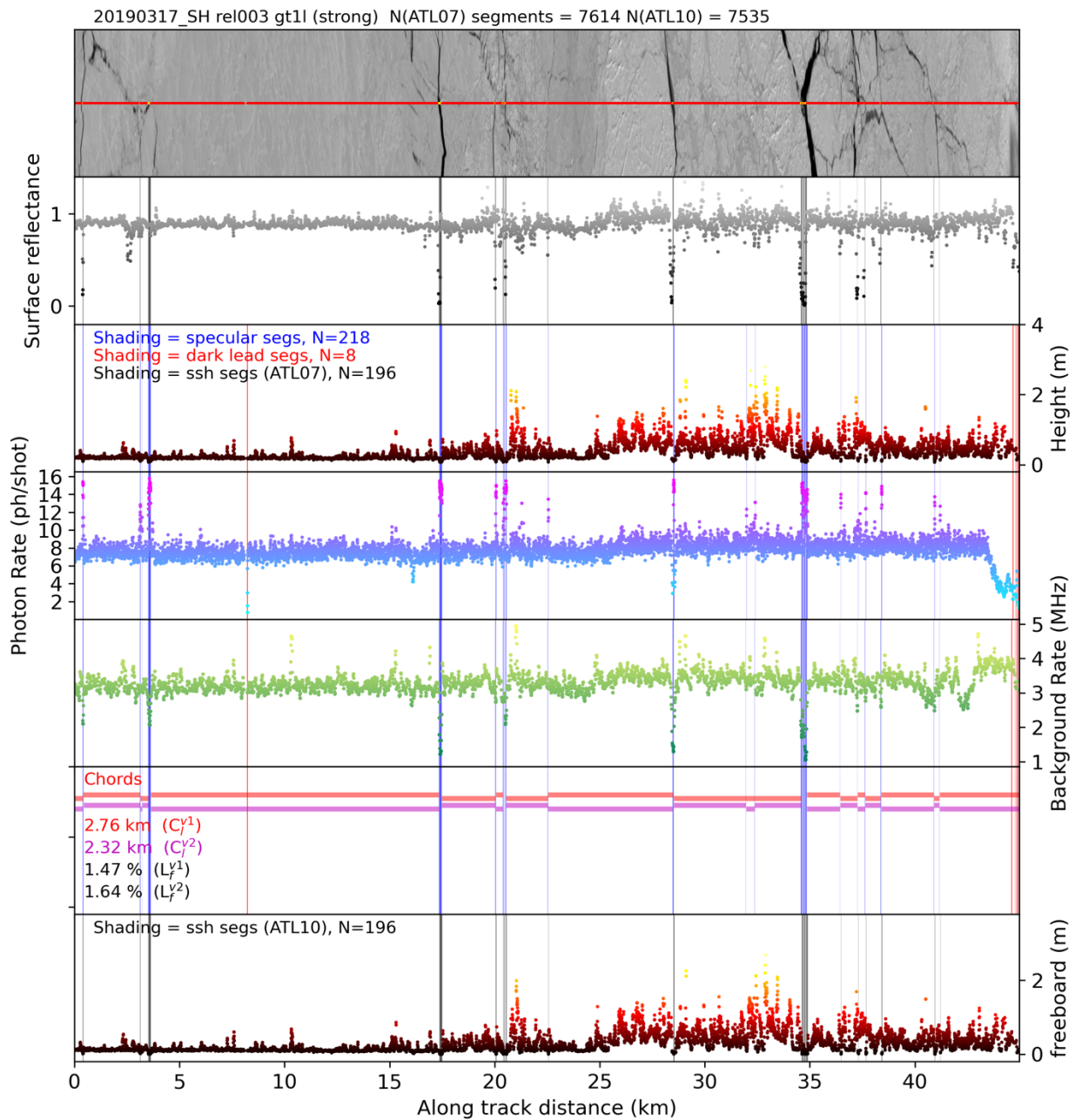


558

559 **Figure 1:** (bottom left) ICESat-2 ATL07 data overlaid on Sentinel-2 RGB image for near-
 560 coincident overpass in the (left column) Western Weddell Sea, Southern Ocean, on March 17th,
 561 2019 and (right column) Lincoln Sea of the Arctic Ocean on May 25th, 2019. The time
 562 difference between the ICESat-2 and Sentinel-2 overpass for the Weddell Sea scene is ~7

563 minutes (ICESat-2 acquisition at 12:29 UTC, Sentinel-2 acquisition at 12:22 UTC), time
 564 difference for the Lincoln Sea scene is ~94 minutes (ICESat-2 acquisition at 00:36 UTC on 26
 565 May 2019, Sentinel-2 acquisition at 23:01 UTC on 25 May 2019). Red segments are classified as
 566 sea ice (*ssh_flag* = 0), yellow segments are classified as leads (*ssh_flag* ≥ 1). The ICESat-2
 567 footprint is not to scale.

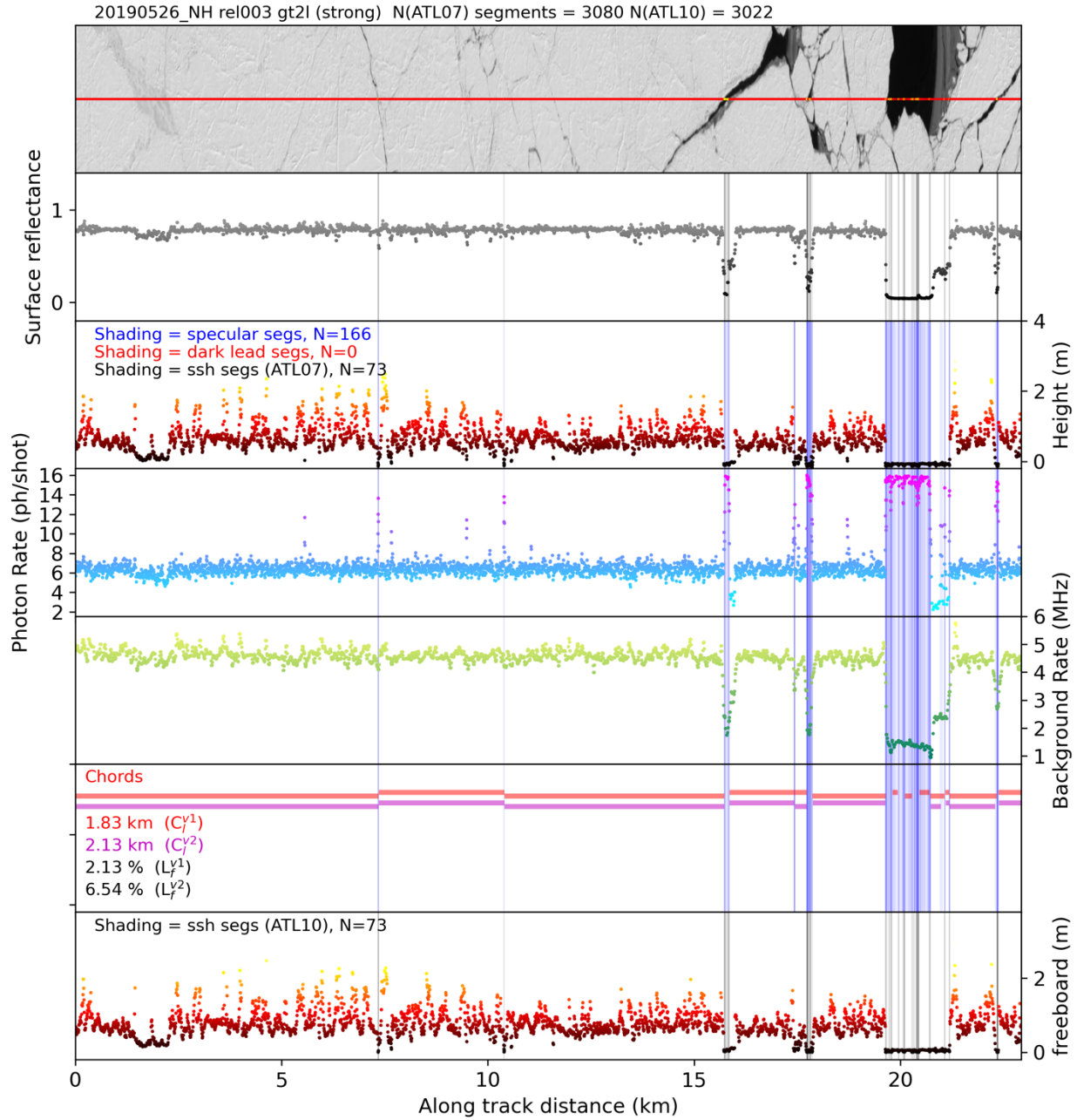
568



569

570 **Figure 2:** ICESat-2 ATL07 data from the strong beam *gt11* overlaid on Sentinel-2 RGB imagery
571 for a ~ 50 km profile in the Western Weddell Sea on March 17th, 2019 (see Figure 1 for
572 location). (top panel) Sentinel image with ICESat-2 profile overlaid showing the sea surface flag
573 (*ssh_flag*, red = ice, yellow = sea surface); (second panel) surface reflectance calculated from the
574 red band of the Sentinel-2 image from nearest neighbor pixels to the ICESat-2 profile; (panels 3-
575 5) segment height, photon rate and background rate respectively from ATL07. Grey shading in
576 panels 2-3 indicate candidate leads (*ssh_flag* = 1) while in panels 4-5, blue shading indicates
577 specular lead classifications (*height_segment_type* = 2 to 5) and red shading indicates dark lead
578 classifications (*height_segment_type* = 6 to 8). Panel 7 shows the derived chord lengths as
579 horizontal bars (red = v_1 , magenta = v_2) with each chord grouping shifted vertically to indicate
580 the groups, and statistics of the mean chord lengths and lead fractions using these two
581 approaches. Panel 8 shows the freeboard in ATL10, with the shading indicating actual leads used
582 to derive reference sea surface (*ssh_flag* = 2). N indicates the number of segments in ATL07 and
583 ATL10 as specified.

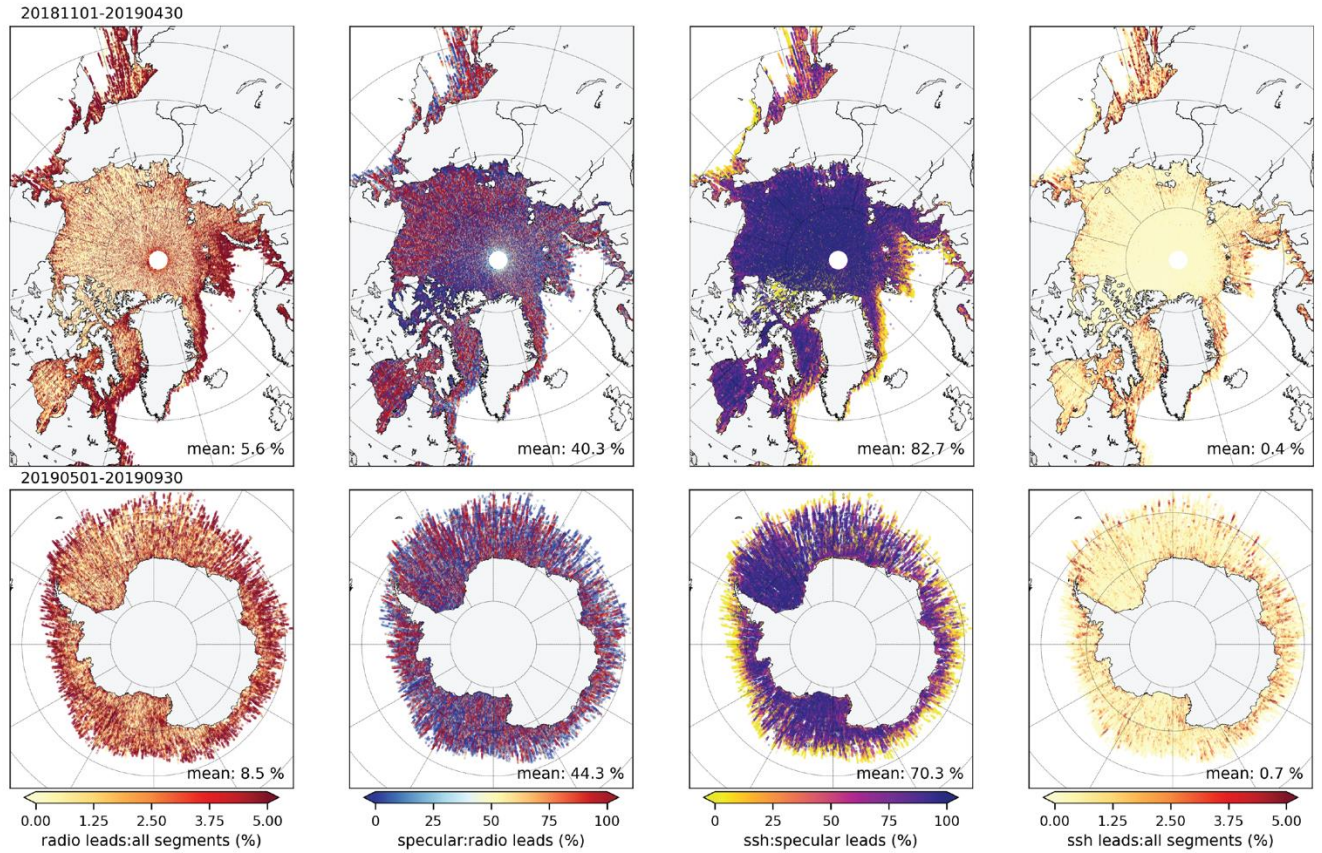
584



585

586 **Figure 3:** As in Figure 2 but for a profile in the Lincoln Sea of the Arctic Ocean on May 26th,
 587 2019 for the strong beam *gt2l* (see map in Figure 1).

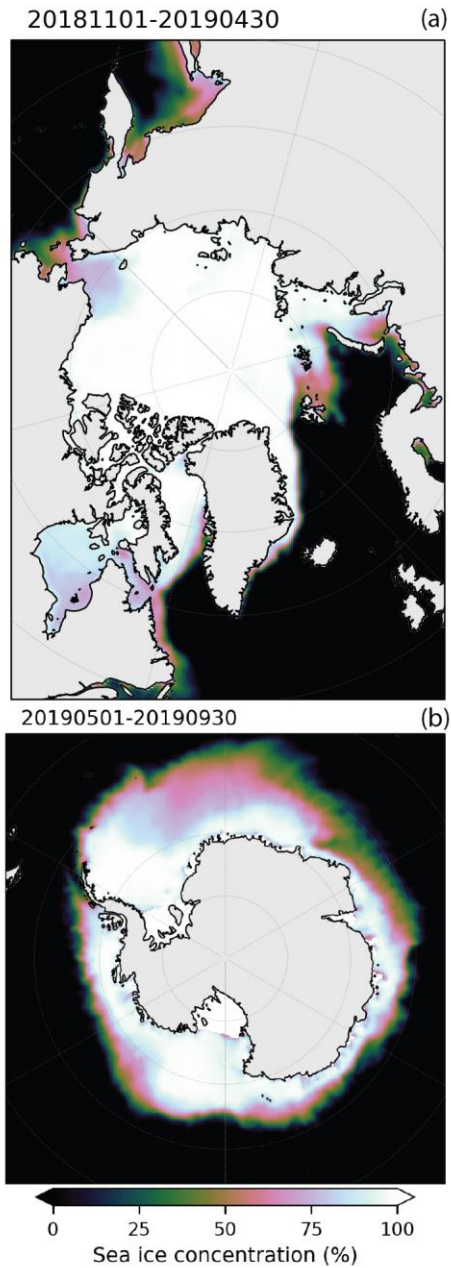
588



589

590 **Figure 4:** (first column) percent of all ATL07 segments classified as radiometric leads
 591 (*height_segment_type* = 2 to 9), (second column) percent of radiometric leads classified as
 592 specular (*height_segment_type* = 2 to 5), (third column) percent of specular leads that become
 593 sea surface segments (*ssh_flag* \geq 1), (fourth column) percent of all height segments that become
 594 sea surface segments. (Top row) Arctic Ocean, November 1 to April 30, 2019, (bottom row)
 595 Southern Ocean, May 1 to September 30, 2019. All these percentages are calculated in 10 km
 596 along-track sections across the three strong beams and are segment length weighted.

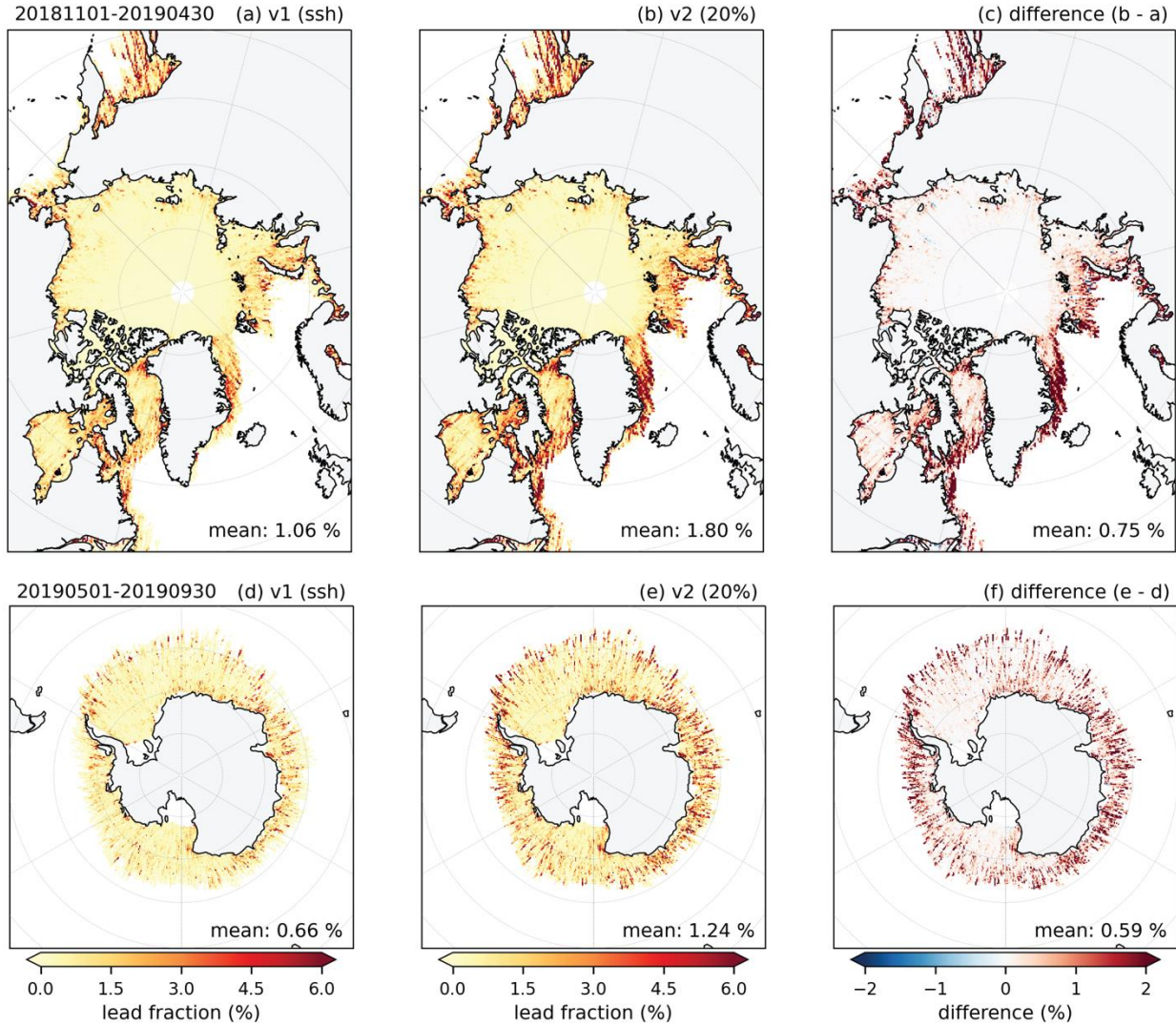
597



598

599 **Figure 5:** Mean winter sea ice concentration derived from passive microwave data (Climate
600 Data Record, CDR) for the (top) Arctic Ocean, November 1, 2018 to April 30, 2019 and
601 (bottom) Southern Ocean, May 1 to September 30, 2019.

602



603

604

Figure 6: Lead fraction using (left) the *ssh_flag* (L_f^{v1}) and (middle) using the higher 20% height

605

filter (L_f^{v2}) and the difference (b minus a) on the right. Data are for the (top) Arctic Ocean,

606

November 1 to April 30, 2019, (bottom) Southern Ocean, May 1 to September 30, 2019. All the

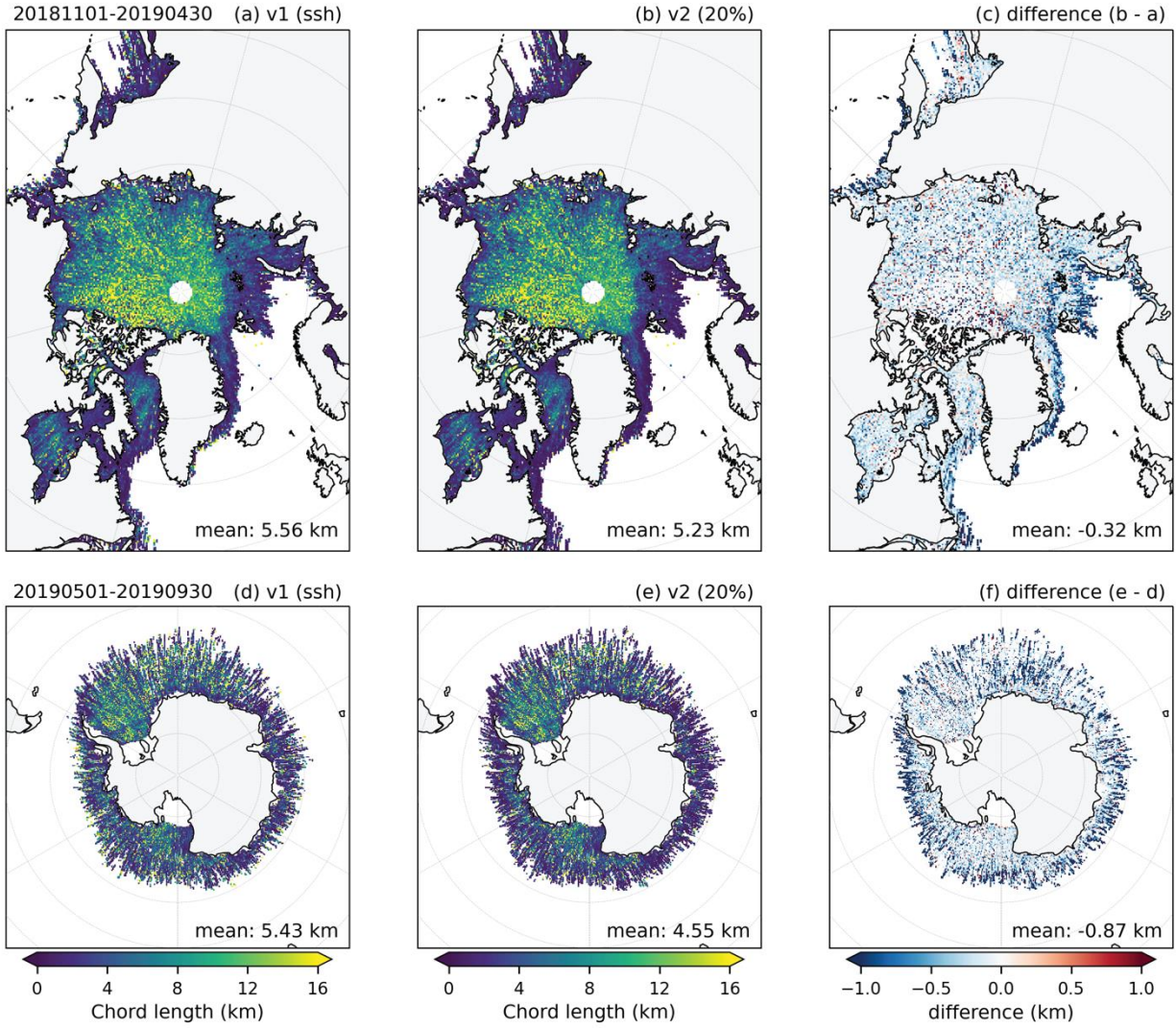
607

fractions are calculated in 10 km along-track sections and are segment length weighted. Data

608

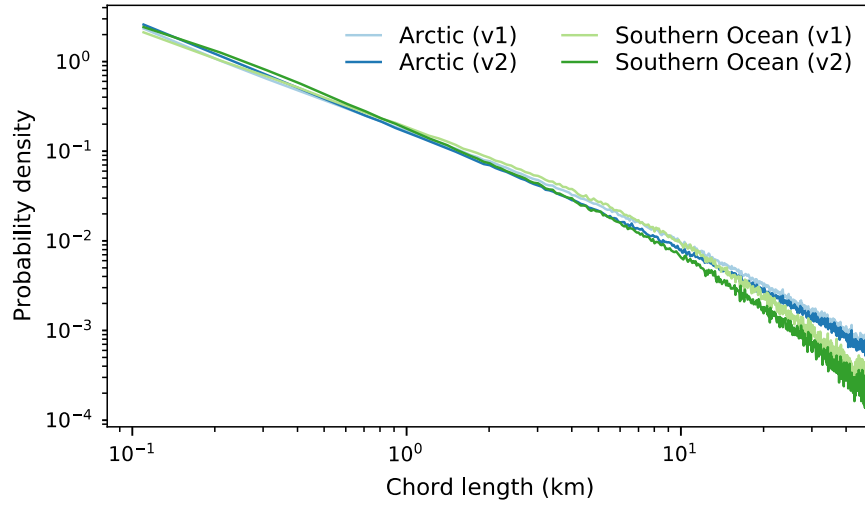
have binned to a 25 km x 25 km polar stereographic grid.

609



610

611 **Figure 7:** As in Figure 5 but for chord length (left) C_l^{v1} and (middle) C_l^{v2} and difference (right).



612

613 **Figure 8:** Probability distributions of the Arctic and Southern Ocean chord lengths (v1: C_l^{v1} and
614 v2: C_l^{v2}) for the same winter-time periods as in Figure 7. Distributions are plotted on a log-log
615 scale.

616